

PAPER

[View Article Online](#)
[View Journal](#) | [View Issue](#)Cite this: *J. Mater. Chem. A*, 2020, **8**, 2644Graphitic carbon nitride doped SnO₂ enabling efficient perovskite solar cells with PCEs exceeding 22%†Jinbo Chen,^a Hua Dong,^a  ^{a,d} Lin Zhang,^a Jingrui Li,  ^c Fuhao Jia,^b Bo Jiao,^{ac} Jie Xu,^a Xun Hou,^a Jian Liu  ^{*b} and Zhaoxin Wu  ^{*ad}

The energy level alignment and carrier mobility of the charge transport layer are of crucial importance for electron extraction and transport in planar heterojunction perovskite solar cells (PSCs). In this work, a carbon nitride modified SnO₂ nanocomposite, SnO₂/graphitic carbon nitride (g-C₃N₄) quantum dots, was designed as the functional electron transport layer (ETL) to precisely regulate the interfacial charge dynamics for high-performance PSCs. It is demonstrated that the g-C₃N₄ could recast the electronic density distribution around the neighboring SnO₂ crystal unit, thus effectively eliminating the oxygen-vacancy-reduced trap centers and promoting the interface and bulk electron transport. Consequently, this carbon nitride modified SnO₂ nanocomposite exhibits appropriate electrical properties including suitable energy level alignment and high conductivity. Employing the typical hybrid SnO₂-based ETL, a maximum power conversion efficiency (PCE) of 22.13% ($V_{oc} = 1.176$ V, $J_{sc} = 24.03$ mA cm⁻², FF = 0.783) can be achieved for planar heterojunction PSCs, with negligible hysteresis and long-term stability (only 10% PCE decay after 1500 h at a relative humidity of 60%). Our work offers a hybrid ETL design strategy to improve the efficiency and stability of PSCs.

Received 15th October 2019
Accepted 25th December 2019

DOI: 10.1039/c9ta11344d

rsc.li/materials-a

Introduction

Organic-inorganic hybrid perovskites have recently attracted enormous interest in the photovoltaic field due to their low exciton dissociation energy, large charge diffusion length and bipolar carrier properties. The efficiency of perovskite solar cells (PSCs) has risen from 3.8% to 25.2% *via* crystal growth control, device architecture optimization, composition engineering and interface engineering.^{1–15} The outstanding performance of PSCs is closely related to the optoelectrical properties of each of the functional layers, including the light-absorbing layer, the electron transport layer (ETL) and the hole transport layer (HTL). Various metal oxides and organic materials with a wide

bandgap and a good transmittance have been developed for the ETL of PSCs, such as fullerene derivatives, TiO₂ and ZnO. However, on the one hand, the low electron mobility and high costs of organic ETLs are not compatible with the commercialization of PSCs. On the other hand, representative metal oxides were reported with the challenges of high-temperature process (TiO₂) or illumination-induced perovskite decomposition (ZnO).^{16–21}

Recently, SnO₂ has been demonstrated as an alternative material for the ETL of PSCs owing to its excellent optical and electrical properties.²² The bandgap of SnO₂ (>3.6 eV, wider than those of TiO₂ and ZnO) could guarantee efficient light-harvesting as well as stability under UV illumination. Meanwhile, the higher electron mobility of SnO₂ could ensure faster charge extraction from the photoactive perovskites. Although SnO₂ exhibits multiple advantages compared with conventional organic and metal oxide materials, the inevitable interface problems and intrinsic defects of SnO₂ still need to be addressed. For the first issue, the imperfect energy-band match could lead to energy loss and charge accumulation at the interface.^{23,24} For the second, localized crystal-induced defects (bulk oxygen vacancies, bulk tin interstitial, surface reconstructions and surface defects) always appeared due to its intrinsic crystallization properties in both vapor-deposition and solution-process developed SnO₂-ETLs.^{25–29} They introduce trap states into the material which can capture electrons and cause the electronic properties of SnO₂ to deteriorate, thus leading to

^aKey Laboratory for Physical Electronics and Devices of the Ministry of Education, Shaanxi Key Lab of Information Photonic Technique, School of Electronic and Information Engineering, Xi'an Jiaotong University, No. 28, Xianning West Road, Xi'an, 710049, China. E-mail: donghuaxjtu@mail.xjtu.edu.cn; zhaoxinwu@mail.xjtu.edu.cn

^bCollege of Materials Science and Engineering, Qingdao University of Science and Technology, Qingdao 266042, China. E-mail: liujian@qust.edu.cn

^cElectronic Materials Research Laboratory, Key Laboratory of the Ministry of Education, International Center for Dielectric Research, School of Electronic Science and Engineering, Xi'an Jiaotong University, Xi'an 710049, People's Republic of China

^dCollaborative Innovation Center of Extreme Optics, Shanxi University, Taiyuan 030006, China

† Electronic supplementary information (ESI) available. See DOI: 10.1039/c9ta11344d

poor charge transport and serious recombination at the perovskite/ETL interface.

Up to now, many efforts have been put into solving the interfacial or bulk problem for SnO_2 . Xie *et al.* demonstrated a new pathway to improve the performance of SnO_2 through graphene quantum dots (GQDs) and SnO_2 composite film, from which the photogenerated electrons in GQDs can transfer to the conduction band of SnO_2 and increase the Fermi level, thus reducing the charge recombination at the ETL/perovskite interface.^{30–34} Tu *et al.* proposed a molecular doping mechanism for n-doping of SnO_2 that could reduce the energy barrier at the perovskite/ SnO_2 interface which favors the PCE increase.³⁵ Generally, doping metal oxides with metals is an efficient way to improve the electronic and interfacial properties of these materials. Hence, aluminum (Al), niobium (Nb), gallium (Ga), lithium (Li), yttrium (Y), and stibium (Sb) doping have been successfully applied to SnO_2 , improving the conductivity of SnO_2 and with it the device PCE.^{36–42} Additionally, organic materials such as ethylene diamine tetraacetic acid, polyethylene glycol and 9-(1-(6-(3,5-bis(hydroxymethyl)phenoxy)-1-hexyl)-1H-1,2,3-triazol-4-yl)-1-nonyl[60] fullerenoacetate^{43–45} have also been used to increase the conductivity of SnO_2 by passivating the surface defects.

In this work, a typical hybrid ETL configuration, SnO_2 /graphitic carbon nitride ($\text{g-C}_3\text{N}_4$) quantum dot nanocomposite (shortened to G- SnO_2 hereafter), was developed to simultaneously solve the interface problem and intrinsic crystal defects of SnO_2 . Therewith, we proposed to endow the PSCs with favorable performance and long-term stability. Benefiting from the sp^2 -hybridization of carbon and nitrogen atoms in $\text{g-C}_3\text{N}_4$, a π -conjugated electronic density distribution can be established around the $\text{g-C}_3\text{N}_4$ / SnO_2 interface; thus, the interaction between the lone-pair electrons of nitrogen and the under-coordinated Sn can effectively passivate the oxygen-vacancy-related defects of SnO_2 . Subsequently, the Fermi level and charge transport of the nanocomposite can be effectively adjusted. Employing the hybrid ETL, a planar heterojunction PSC based on G- SnO_2 shows a champion PCE of 22.13% with an open-circuit voltage (V_{oc}) of 1.176 V, a short-circuit current density (J_{sc}) of 24.03 mA cm^{-2} , and a fill factor (FF) of 0.783. More importantly, benefiting from the trap-healing ability, high corrosion resistance and good chemical stability of $\text{g-C}_3\text{N}_4$, PSCs employing the hybrid G- SnO_2 ETL also exhibit excellent long-term stability, with 90% of the original PCE retained after 1500 h under ambient conditions ($\sim 60\%$ humidity).

Results and discussion

Fig. 1 shows the synthesis and the molecular structure of $\text{g-C}_3\text{N}_4$ quantum dots (g-CNQDs). The synthesis can be divided into two steps, including acid etching with a mixture of H_2SO_4 and HNO_3 to form porous $\text{g-C}_3\text{N}_4$ and hydrothermal treatment with the aid of $\text{NH}_3 \cdot \text{H}_2\text{O}$ to form g-CNQDs. The g-CNQDs feature the sp^2 -hybridized carbon and nitrogen atoms, establishing the π -conjugated electronic structures. Transmission electron microscopy (TEM) images of g-CNQDs are shown in Fig. 2a and b. They show that the size distribution of the as-prepared g-

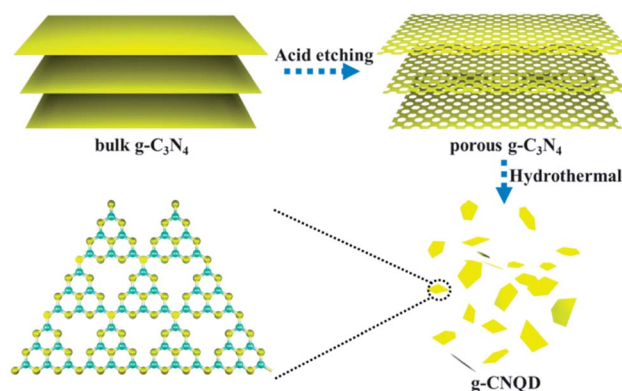


Fig. 1 The synthesis of g-CNQDs and their molecular structure.

CNQDs is very uniform, with a diameter of around 5–10 nm. The lattice spacing of g-CNQDs is 0.336 nm, corresponding to the (002) plane of hexagonal $\text{g-C}_3\text{N}_4$.⁴⁶ Fig. 2c shows the SnO_2 particles with a diameter of around 5 nm and the SnO_2 nanoparticles are polycrystalline.⁴⁷ Fig. 2d shows the arrangement of G- SnO_2 *via* HR-TEM, which reveals that these two materials present a homogeneous mixture and form the functional nanocomposite.

Fig. 3a shows the optical transmission spectra of the glass/ITO substrate coated with SnO_2 and G- SnO_2 films with the same thickness. Both films exhibit high transmittance in the visible region due to the wide bandgap (3.8 eV, Fig. S1†) of g-CNQDs, which could enable sufficient light-capturing of PSCs. The absorption spectra of SnO_2 and G- SnO_2 are shown in Fig. S2.† To study the effect of the hybrid ETL on the quality of perovskite film, we analyzed the crystal structure and morphology of perovskite films deposited on SnO_2 and G- SnO_2 substrates. Fig. 3b shows the XRD patterns of perovskite films

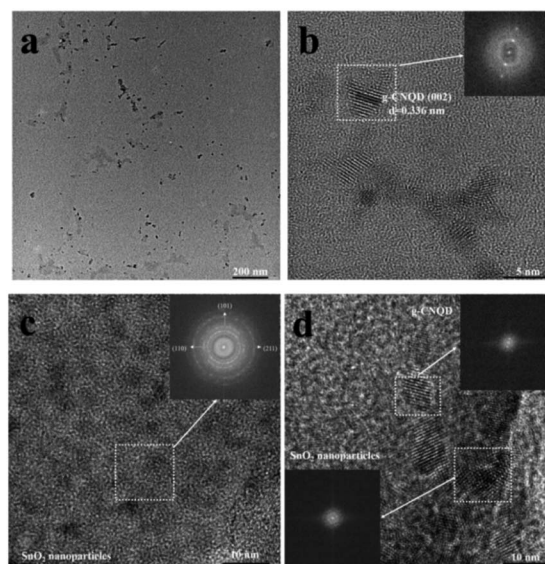


Fig. 2 (a and b) TEM micrographs of the as-prepared g-CNQDs. (c and d) TEM images of the SnO_2 nanoparticles and G- SnO_2 . The inset images show the FET transition.

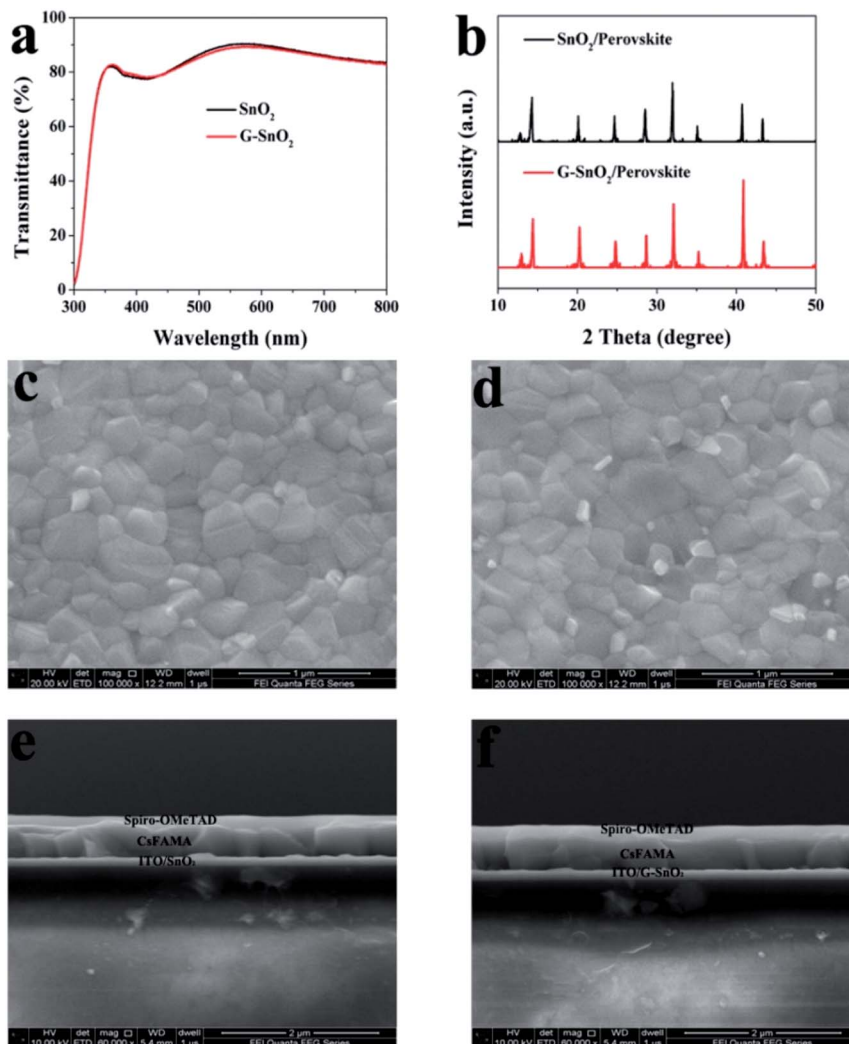


Fig. 3 (a) The transmission spectra of SnO₂ films and G-SnO₂ deposited on an ITO glass substrate. (b) XRD patterns of perovskite deposited on SnO₂ films and the G-SnO₂ substrate. (c and e) The surface and cross-sectional SEM images of perovskite on SnO₂. (d and f) The surface and cross-sectional SEM images of perovskite on G-SnO₂.

on SnO₂ and G-SnO₂. Similar peak positions and peak intensities are observed for both films, and they agree well with the typical black phase of perovskite, thus indicating the same crystallinity. Fig. 3c–f show the top view topographic scanning electron microscope (SEM) images and the corresponding cross-sectional SEM images of perovskite on SnO₂ and G-SnO₂ (the films were prepared using the same composition and process). It is found that both the SnO₂ and G-SnO₂ exhibited good surface wettability (shown in Fig. S3†); thus, high-quality perovskite films can be obtained on either SnO₂ or G-SnO₂ with a dense and uniform morphology. The UV-visible absorption spectra of perovskites on SnO₂ and G-SnO₂ were also measured and are shown in Fig. S4,† also exhibiting no distinct difference in absorption edge. All of this indicates that the change in surface properties upon modification of the ETL has little impact on the optical properties and crystallinity of the *in situ* grown perovskite films.

In this work, the performance of PSCs with g-CNQD modified SnO₂ was demonstrated in a typical normal planar PSC

structure with the basic configuration “ITO/ETL/CsFAMA/Spiro-MeOTAD/Au”, and the schematic diagram is shown in Fig. 4. To further investigate the effect of the g-CNQDs on device performance, g-CNQDs with a series of concentrations were incorporated into SnO₂ films. Fig. 5a shows the *J*–*V* curves of the representative device in the reverse scan of the bare-SnO₂ based (black) and the G-SnO₂ based (red) devices. The average and best data of *V*_{oc}, *J*_{sc}, FF and PCE of bare SnO₂ and optimal concentration G-SnO₂ are summarized in Table 1 (24 samples for each structure and the statistics listed in in Tables S2 and S3†), and the statistical data of different g-CNQD doping concentration PSCs are shown in Fig. S5.† With the concentration of the g-CNQDs increased, an increase-to-decrease tendency of device PCE was observed. Here all types of devices show good repeatability of performance as typical *J*–*V* curves (Fig. S6†). The G-SnO₂ based devices show much higher reproducibility, with a small relative PCE standard deviation of 0.37%, which is lower than that of the bare-SnO₂ PSCs (0.41%). The best PCE is remarkably improved from 20.21% to 22.13%,

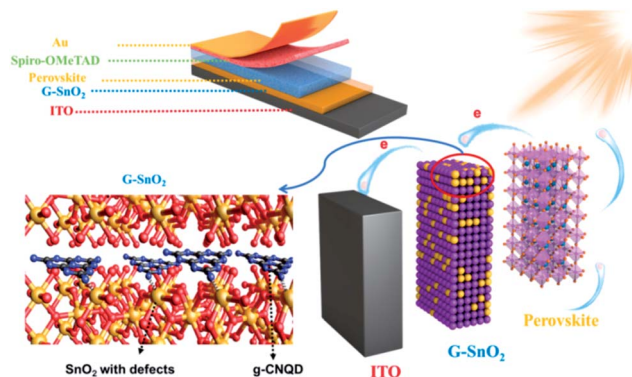


Fig. 4 The schematic diagram of the G-SnO₂ based PSC.

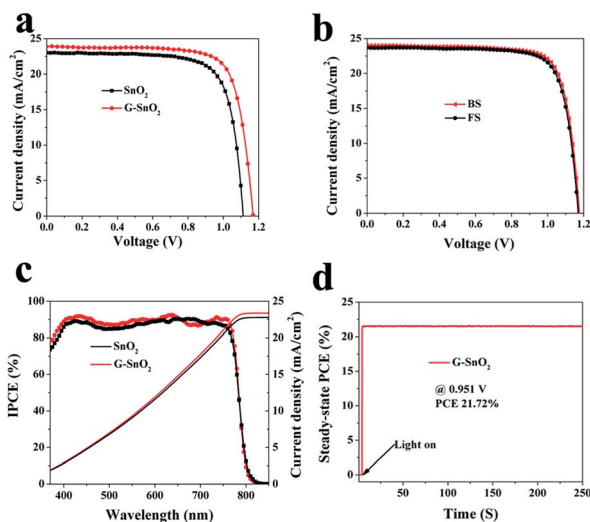


Fig. 5 (a) The J - V curves of the SnO₂ and G-SnO₂ PSCs. (b) The J - V curves of G-SnO₂ PSCs in both forward and reverse scan directions. (c) The IPCE curves of the SnO₂ and G-SnO₂ PSCs. (d) The steady-state PCE test of the device fabricated with G-SnO₂ at maximum power output point.

V_{oc} from 1.118 to 1.176 V, FF from 0.762 to 0.783, and J_{sc} from 23.72 to 24.03 mA cm⁻². Fig. 5b shows the best J - V characteristics of the device with G-SnO₂ in both reverse and forward scan directions. The device showed a V_{oc} of 1.176 V, J_{sc} of 24.03 mA cm⁻², FF of 0.783 and PCE of 22.13% under the reverse scan, while showing a V_{oc} of 1.169 V, J_{sc} of 23.68 mA cm⁻², FF of 0.781, and PCE of 21.61% under the forward scan, with negligible hysteresis. Fig. 5c shows the external quantum efficiency (EQE) spectra of the bare-SnO₂ and G-SnO₂ PSCs, as well as the integrated current density which is in good agreement with the J_{sc} from the J - V results. Compared with bare-SnO₂ PSCs, G-SnO₂

PSCs showed a relatively higher EQE, explaining their higher photocurrent. The steady-state conversion efficiency obtained from the i - t curve was 21.72% (at maximum power output point), which approaches an average efficiency of 21.87% measured from the forward and reverse scanning J - V curves.

Based on the film characteristics, the improvement and variation of the device performance should be attributed to the essential interfacial/bulk electrical properties of the modulated ETL, and are suspected to reflect the two sides of g-CNQDs, that is, the competition of defect passivation and dissatisfactory conductivity. To verify this, firstly, the electron mobility is measured using electron-only devices using space-charge-limited-current (SCLC). The details are shown in Fig. S7 and Table S4.† Benefiting from the trap-passivation ability of g-CNQDs, the electron mobility of G-SnO₂ is increased from 5.2×10^{-3} to 7.5×10^{-3} cm² V⁻¹ s⁻¹ upon 3 mg ml⁻¹ g⁻¹-CNQD doping. And then upon continued increase of the g-CNQD concentration to 5 mg ml⁻¹, the electron mobility decreased to 5.34×10^{-3} cm² V⁻¹ s⁻¹, due to the excessive g-CNQDs with dissatisfactory conductivity obstructing the charge transporting capability of the modified ETL, while the oxygen vacancy defects of the SnO₂ films are sufficiently healed. Here the electron mobility change tendency is in accord with the increase-to-decrease tendency of device PCE.

To further investigate the influence of g-CNQD doping, the conductivity, charge transfer, intrinsic defect evolution and band alignments of bare SnO₂ and optimal concentration G-SnO₂ were systematically investigated through experimental and theoretical studies. Fig. 6a shows the electrical conductivity of the two types of ETLs deposited on ITO substrates. Obviously higher electrical conductivity was observed in the G-SnO₂ sample, which originates from the passivation of defects in SnO₂.⁴⁸ Fig. 6b shows the Mott-Schottky plots of the SnO₂ and G-SnO₂ devices. The doping density can be derived using the following equation:

$$\frac{1}{C^2} = \frac{2}{\epsilon \epsilon_0 q A^2 N} (V_{fb} - V)$$

where C represents the measured capacitance, A is the active area, V is the applied bias, ϵ is the static permittivity, ϵ_0 is the vacuum permittivity, q is the elementary charge, and N is the doping density. A doping density increase from 5.76×10^{17} cm⁻³ to 8.10×10^{17} cm⁻³ was observed, corresponding to the enhanced conductivity of the modified SnO₂.⁴⁹ To analyze the charge transfer characteristic at the perovskite/ETL interface, time-resolved photoluminescence (TRPL) of perovskite on SnO₂ and G-SnO₂ was measured as shown in Fig. 6c, and the corresponding fitting parameters are listed in Table S1.† Generally, the fast decay component (τ_1) is attributed to the quenching of charge carriers at the interface, and the slow decay component

Table 1 Parameters of the perovskite solar cells; data in parentheses represent the maximum value

| | V_{oc} (V) | J_{sc} (mA cm ⁻²) | FF | PCE (%) |
|--------------------|-----------------------|---------------------------------|-----------------------|-----------------------|
| SnO ₂ | 1.114 ± 0.007 (1.118) | 23.44 ± 0.195 (23.72) | 0.749 ± 0.011 (0.762) | 19.56 ± 0.405 (20.21) |
| G-SnO ₂ | 1.163 ± 0.006 (1.176) | 23.88 ± 0.140 (24.03) | 0.764 ± 0.010 (0.783) | 21.24 ± 0.370 (22.13) |

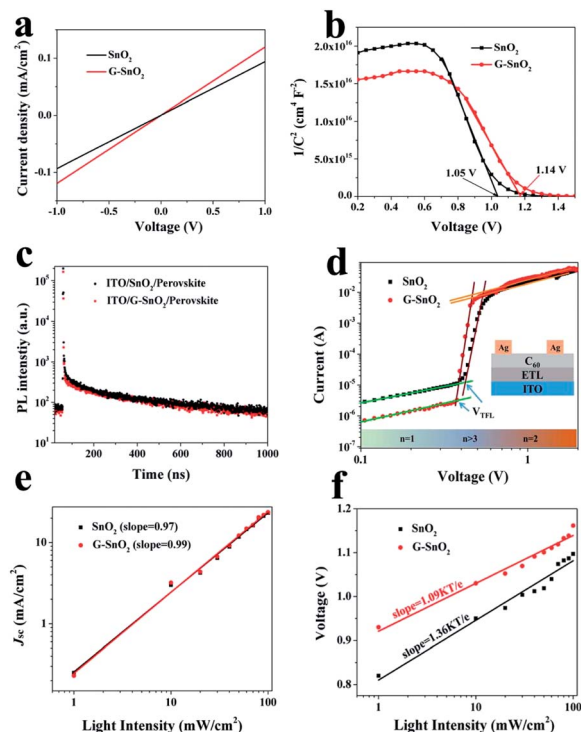


Fig. 6 (a) J - V characteristics of the ITO/SnO₂ and G-SnO₂/Ag devices in the dark. (b) Mott-Schottky plots of the SnO₂ and G-SnO₂ devices. (c) The TRPL of perovskite on SnO₂ and G-SnO₂. (d) The I - V curves of electron-only devices with the structure of ITO/ETL/C₆₀/Ag. (e) J_{sc} and (f) V_{oc} dependence upon different light intensities.

(τ_2) originates from the radiative recombination of free charge carriers in the bulk.⁵⁰ For τ_1 , a significant decrease from 42.05 ns (bare-SnO₂) to 12.7 ns (G-SnO₂) was observed, which indicates enhanced charge transfer from perovskite to the G-SnO₂ layer.

Oxygen vacancies are inevitably formed in the as-prepared SnO₂ materials, which could act as charge traps in the SnO₂ films and be unfavorable for electron transport. Considering that the carbon and nitrogen atoms of g-C₃N₄ are sp²-hybridized and establishing the electronic structures of π -conjugation, we hypothesized that the excess oxygen vacancies in SnO₂ could be consumed under the electron-rich conditions. Electron-only devices with the structure of ITO/ETL/C₆₀/Ag were fabricated to evaluate the electron trap density of both bare-SnO₂ and G-SnO₂ films. Fig. 6d shows the current-voltage (J - V) curves of the electron-only devices. The linear correlation reveals an ohmic-type response at low bias voltage; as the voltage is continuously increased, this square-law region will be terminated in a steeply rising current due to the trap filling. The trap density (N_t) can be obtained using the following equation:

$$N_t = \frac{2\varepsilon_0\varepsilon V_{TFL}}{eL^2}$$

where e is the elementary charge and L is the thickness of the film.⁴³ The electron trap densities of the SnO₂ and G-SnO₂ substrates are $2.57 \times 10^{16} \text{ cm}^{-3}$ and $2.05 \times 10^{16} \text{ cm}^{-3}$, respectively. The lower electron trap density in the G-SnO₂ bulk,

naturally also at the G-SnO₂/perovskite interface, will reduce the trap-mediated carrier recombination and increase the V_{oc} . Fig. S8† shows the Nyquist plots of the devices employing bare SnO₂ and G-SnO₂ ETLs. The semicircles in the low and high frequency regions are attributed to the recombination resistance (R_{rec}) and the transfer resistance (R_{tr}), respectively. The fitting results of R_{rec} are $8.5 \times 10^4 \Omega$ and $1.1 \times 10^5 \Omega$, and those of R_{tr} are $4.2 \times 10^4 \Omega$ and $3.9 \times 10^4 \Omega$, for SnO₂ and G-SnO₂, respectively. The larger R_{rec} and smaller R_{tr} of the device with the G-SnO₂ ETL correspond to the more efficient charge extraction and suppressed charge recombination at the interface, thus resulting in the device-performance improvement.

More direct insight into the recombination kinetics within the device can be obtained by measuring J_{sc} and V_{oc} at various light intensities. Monomolecular recombination refers to any first-order process including the geminate recombination of a bound electron-hole pair before dissociation and the Shockley-Read-Hall (SRH) recombination at the shallow traps created by defects and impurities in the interfacial layer, while bimolecular recombination refers to the recombination of free electrons and holes in the photoactive layer.^{51,52} Fig. 6e presents the dependence of J_{sc} on the incident light intensity (I) on a logarithmic scale according to $J_{sc} \propto \alpha I$, from which the slopes of the bare SnO₂ and G-SnO₂ devices are 0.97 and 0.99, respectively. At $\alpha = 1$, all carriers are swept out prior to recombination. The slightly larger (closer to 1) slope of the G-SnO₂ device indicates that the bimolecular recombination during sweeping out the carriers is suppressed at the G-SnO₂/perovskite interface when compared with the bare-SnO₂-based control device, which is due to the much more efficient carrier extraction and transport. Besides, the dependence of V_{oc} on the logarithm of the incident light intensity ($\log(I)$) is shown in Fig. 6f, and can be fitted according to the equation $V_{oc} = \varepsilon kT \ln(I)/e + \text{constant}$, where ε is the ideality factor, k is the Boltzmann constant and T is the temperature. For monomolecular recombination, V_{oc} versus $\ln(I)$ would be $2kT/e$. The value between kT/e and $2kT/e$ indicates the presence of bimolecular recombination and monomolecular SRH recombination.^{53,54} As shown in Fig. 6f, the G-SnO₂-based PSC possesses a weaker V_{oc} dependence on the light intensity ($1.09kT/q$) than the bare-SnO₂-based device ($1.36kT/q$), demonstrating that G-SnO₂ effectively reduces the monomolecular SRH recombination (interfacial trap-assisted recombination), which is largely attributed to a reduction of defect density, resulting in improved device performance.

X-ray photoelectron spectroscopy (XPS) was utilized to analyze the core-level chemical shift of tin. As shown in Fig. 7a and S9,† the signal peaks of Sn 3d at 486.4 eV and 494.9 eV correspond to the featured bonds of Sn 3d_{3/2} and Sn 3d_{5/2}, respectively. In addition, the signal peaks of Sn 3d in G-SnO₂ shift slightly to higher binding energies at 486.6 eV and 495.0 eV. The blue shift (toward higher binding energy) of Sn 3d demonstrates electron transfer from g-CNQDs to the surface tin atoms.³⁵ To investigate the change of band positions induced by g-CNQD incorporation, ultraviolet photoelectron spectroscopy (UPS) of SnO₂ and G-SnO₂ was performed and the results are shown in Fig. 7b. The Fermi levels (E_F) of SnO₂ and G-SnO₂ are calculated to be -4.85 eV and -4.55 eV , using the formula $E_F =$

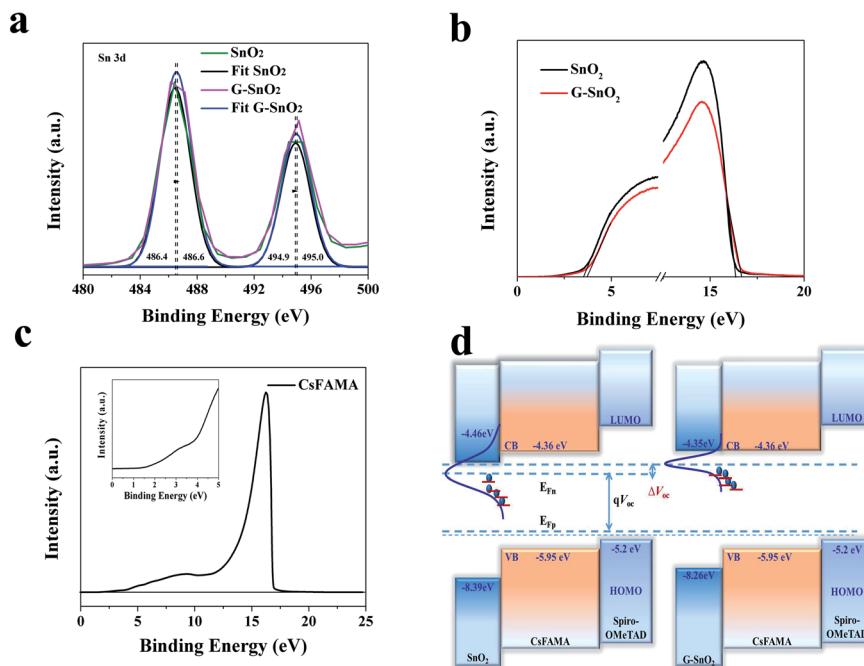


Fig. 7 (a) XPS core-level spectra of Sn 3d on SnO₂ and G-SnO₂ films. (b) UPS spectra of SnO₂ and G-SnO₂ films. (c) UPS spectra of CsFAMA perovskite film. (d) Possible band alignment of the ETL, HTL and perovskite layer according to their conduction band.

21.22 eV – $E_{\text{cut-off}}$ (cut-off binding energy). From Fig. 7b the E_{VBM} of SnO₂ and G-SnO₂ was determined to be –8.39 eV and –8.26 eV, respectively, using $E_{\text{VBM}} = E_{\text{F}} - E_{\text{F,edge}}$ (Fermi edge). The bandgap (E_{g}) of SnO₂ and G-SnO₂ is found to be 3.91 eV from the Tauc plot, showing that the g-CNQD dopant did not affect E_{g} (Fig. S2†). E_{CBM} is determined from E_{g} and E_{VBM} , which

are found to be –4.48 eV and –4.35 eV, respectively, as depicted in Fig. 7d. Due to the shift of the work function and the change in the surface electron density of SnO₂ after g-CNQD doping, the energy band alignment at the perovskite/G-SnO₂ interface is expected to be more favorable. The UPS and absorption measurements of mixed cation CsFAMA perovskite are also

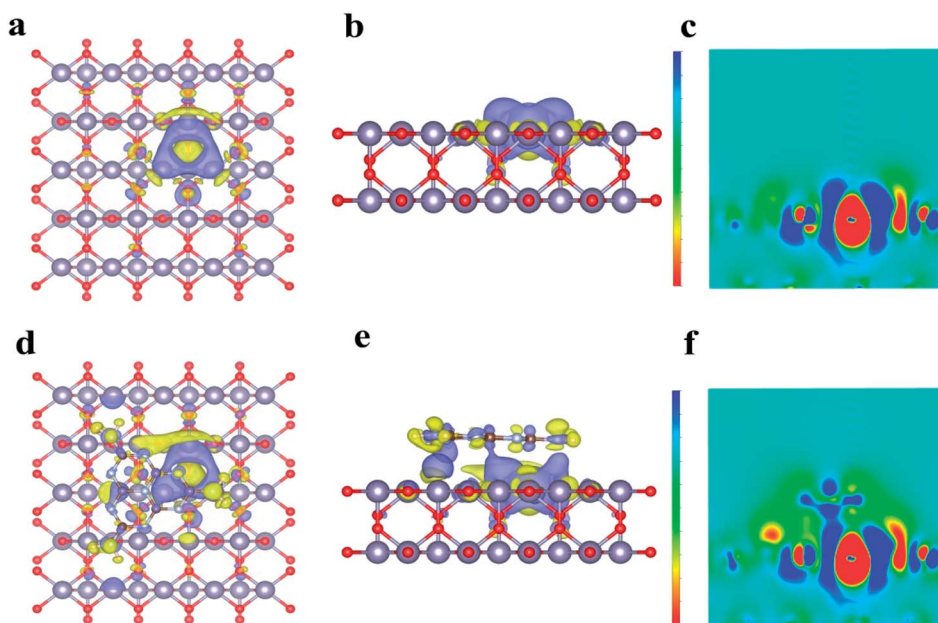


Fig. 8 (a and d) The top view of the charge density difference of SnO₂ and G-SnO₂ with an oxygen vacancy. (b and e) The side view for the charge density difference of SnO₂ and G-SnO₂ with an oxygen vacancy. The cyan and yellow areas indicate electron accumulation and depletion, respectively. (c and f) The corresponding 2D view of the oxygen vacancy plane; the blue and red areas indicate electron accumulation and depletion, respectively.

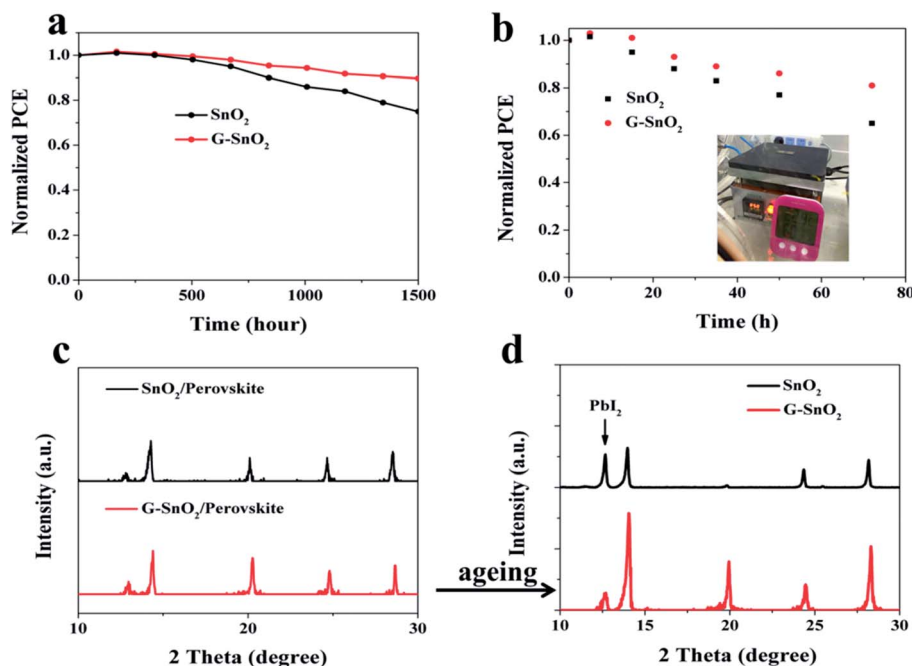


Fig. 9 (a) PCE changes of the SnO₂ and G-SnO₂ PSCs under dark conditions (60% relative humidity at 25 °C), and (b) PCE changes of the unencapsulated SnO₂ and G-SnO₂ PSCs (60% relative humidity at 85 °C); the inset picture shows the test conditions. (c and d) XRD patterns of perovskite deposited on the SnO₂ film and G-SnO₂ substrate before and after ageing at 85 °C and 60% relative humidity for 72 hours.

obtained as shown in Fig. 7c and S4,[†] and the E_F , E_{CBM} and E_{VBM} are -4.41 , -4.36 and -5.95 eV, respectively. The energy band level alignments of SnO₂ and G-SnO₂ with the perovskite layers deposited on them are shown in Fig. 7d. According to the basic theory of band alignment of heterojunctions, the band bending of each material at the perovskite/SnO₂ interface leads to an energy barrier at the interface, which then suffers from charge accumulation and energy loss.^{49,55} Although the E_{CBM} of G-SnO₂ is slightly higher (0.01 eV) than that of CsFAMA, considering the multiple factors (interface traps and energy band alignment) influencing the interface extraction/transporting efficiency, the electron transporting behavior at the ETL/perovskite interface could be improved in G-SnO₂ based PSCs. At the same time, the V_{oc} in a photovoltaic device is determined by the quasi-Fermi level splitting of electrons and holes in the whole device under illumination, which is affected by the occupation of the available electronic states by photogenerated charge carriers, not only in the perovskite layer but also in the charge transport layers. Thus, the E_F upshift of the ETL can also increase the quasi-Fermi level splitting of electrons and holes and enlarge the V_{oc} , in accordance with the G-SnO₂ devices demonstrating a higher flat-band potential in the Mott-Schottky plots (Fig. 6b).^{36,48}

To verify our speculation and gain insight into the charge density distribution of SnO₂ and G-SnO₂ with oxygen vacancies, density functional theory (DFT) calculations were carried out for both systems using the Vienna *Ab initio* Simulation Package (VASP).^{56,57} The Perdew–Burke–Ernzerhof generalized gradient approximation was used as the exchange–correlation functional in combination with the projector augmented wave method and the DFT-D3 method to incorporate the van der Waals

interactions between the g-C₃N₄ molecule and the SnO₂ (110) surface.^{58,59} Adsorption configurations of g-C₃N₄ on the SnO₂ (110) surface with and without an oxygen vacancy concentration of 1/217 were considered. Details of our DFT calculations are available in the Experimental section of the ESI.[†] The DFT-calculated charge density difference of SnO₂ with an oxygen vacancy is shown in Fig. 8a and b. The cyan region represents charge accumulation, and the yellow region indicates charge depletion. It is clearly seen that the center of the oxygen vacancy shows intense electron depletion and the three Sn atoms surrounding the vacancy show electron accumulation. So the oxygen vacancy is positively charged, always as the electron trap center. The charge density difference of G-SnO₂ with an oxygen vacancy is shown in Fig. 8d and e. As shown, the charge redistribution occurred around the oxygen vacancy, and there was clear interaction between the g-C₃N₄ and the three Sn atoms surrounding the vacancy; the interaction can be seen more clearly in the 2D views in Fig. 8c and f. As a result of g-C₃N₄ doping, the number of delocalized electrons on Sn atoms around the oxygen vacancy is remarkably augmented after the absorption of g-C₃N₄. This calculation result confirms our speculation of oxygen vacancy defect passivation and that the signal peaks of Sn 3d shift. The charge density difference of G-SnO₂ was also calculated (Fig. S10[†]). Charge redistribution at the SnO₂(110)/g-C₃N₄ interface region is observed. The change at the interfaces indicated that there is electron transfer from the g-C₃N₄ side to the SnO₂ side across the interface, in accordance with the doping density increase observed in Mott–Schottky plots.^{60–64}

It is known that the stability of perovskite films always poses a challenge for PSC commercialization. The commonly used

TiO₂ ETL has been found to cause a rapid degradation of perovskite film under UV light, because desorption of O²⁻ at oxygen vacancies destroys the interface and perovskite. Compared to TiO₂, low oxygen vacancy density SnO₂ shows much better performance under oxygen and moisture conditions. To study the stability of the device based on a typical hybrid ETL, related investigations on unencapsulated PSCs were carried out. The stability test results are shown in Fig. 9, and the stability test results previously reported using SnO₂ and modified SnO₂ as ETLs are also listed in Table S5.† It is clear that the device based on G-SnO₂ maintains 90% of its initial efficiency after 1500 h when exposed to an ambient atmosphere, and retains 80% of its initial efficiency after ageing for 72 hours under conditions of 60% relative humidity at 85 °C. The XRD patterns of perovskite film after ageing are shown in Fig. 9c and d; the PbI₂ peak of G-SnO₂ is much weaker than that of bare SnO₂. Here the excellent stability of G-SnO₂ based PSCs can be attributed to two aspects: firstly, as a typical carbon nitride material, g-C₃N₄ has the features of excellent corrosion resistance and chemical stability; secondly, the elimination of the surface/bulk defects of SnO₂ could further restrain the material's decomposition, and G-SnO₂ with reduced oxygen vacancies effectively prevents hydroxide adsorption, restraining the material's decomposition.

Conclusions

In summary, we demonstrated an innovative design scheme for the electron transporting layer, that is, a hybrid nanocomposite consisting of g-CNQDs and SnO₂, for applying to PSCs with high performance and long-term stability simultaneously. Theoretical and experimental studies show that with the incorporation of g-CNQDs into SnO₂, charge redistribution could be induced at the SnO₂/g-C₃N₄ interface region for passivating the oxygen vacancies effectively. Correspondingly, the energy band alignment and charge extraction behavior at the ETL/perovskite interface was regulated. As for the best device utilizing the G-SnO₂ hybrid ETL, a favorable 22.13% PCE was obtained compared with the control device with a PCE of 20.21%. Furthermore, the G-SnO₂ based device also presented considerable long-term stability, with 90% of the original efficiency retained after 1500 h ageing (at a humidity of 60%). We think that the explorations in our work could provide a facile ETL-design strategy in the thriving perovskite photovoltaic field.

Experimental details

Materials

N,N-dimethylformamide (DMF), dimethyl sulfoxide (DMSO) and SnO₂ colloid precursor were obtained from Alfa Aesar. Acetonitrile (ACN), bis(trifluoromethanesulfonyl)imide lithium (Li-TFSI), *tert*-butylpyridine (tBP), and CsI were purchased from Sigma-Aldrich. PbI₂ and PbBr₂ were purchased from TCI. MABr and FAI were synthesised following the procedure in previous reports. Spiro-OMeTAD and tris(2-(1*H*-pyrazol-1-yl)-4-*tert*-butylpyridine)-cobalt(III) tris(bis(trifluoromethylsulfonyl)imide) (FK209) were purchased from Xi'an Polymer Light Technology

Corp. Chlorobenzene (CB) was obtained from Acros. All materials above were used as received.

Preparation of SnO₂ and G-SnO₂ precursors

g-CNQD particles were dispersed in 50 ml deionized water, ultrasonicated for 8 hours, and then filtered with a 0.45 µm filter to obtain a g-CNQD water solution. The SnO₂ colloid precursor was diluted with deionized water and g-CNQD water solution in a 1 : 2 ratio, and then ultrasonicated for 2 hours. Then the SnO₂ and G-SnO₂ precursors were obtained.

Device fabrication

ITO glass was cleaned by sequentially washing with detergent, deionized (DI) water, and isopropanol (IPA). Before use, the ITO was cleaned by UVO treatment for 10 min. Then, the substrate was spin-coated with SnO₂ and G-SnO₂ precursors (1500 rpm, 30 s) and baked on a hot plate in ambient air at 180 °C for 30 min. After cooling to room temperature, the substrate was treated by UVO exposure for 15 min. Here, CsFAMA mixed perovskite precursor solution was prepared by mixing PbI₂, PbBr₂, FAI and MABr in DMF/DMSO (v/v: 4/1), where the mole concentration of PbI₂ was kept at 1.3 M with 0.1 M excess, and the mole ratios of I/Br and FA/MA were maintained at 0.85 and 0.15. 47 µl of CsI (1.5 M in DMSO) was added and the resulting mixture was stirred for 3 hours. CsFAMA perovskite films were deposited by spin coating (2000 rpm, 10 s/6000 rpm, 30 s) and 250 µl CB was used as an antisolvent 15 s prior to the end of the spinning. This was followed by annealing for 1 h at 100 °C. The Spiro-OMeTAD solution was coated at 1500 rpm for 30 s, where 1 ml Spiro-OMeTAD/CB (90 mg ml⁻¹) solution was used, with the addition of 17.8 µl Li-TFSI/ACN (520 mg ml⁻¹), 28.5 µl tBP and 20 µl FK209/ACN (200 mg ml⁻¹). Finally, a Au back electrode was deposited by thermal evaporation. The active area was 0.0706 cm².

Characterization

UPS and XPS measurements were performed on an ESCALAB 250Xi, Thermo Fisher (by using Al K_γ X-ray source) under high vacuum (at a base pressure of 1.0 × 10⁻⁹ torr). For the work function measurements using UPS, a 10 V bias was applied and Au was used as the reference. The XPS spectra were calibrated using the binding energy of C 1s. UV measurements were performed on a UV/Vis/NIR spectrometer (HITACHI U-3010, Japan). *J*-*V* measurements were carried out using a Keithley 2400 sourcemeter in an ambient environment of 24 °C and 30% RH. Illumination was provided by a SAN-EI XES-301S solar simulator with AM1.5G spectrum and the light intensity of 100 mW cm⁻² was calibrated by means of a KG-5 Si diode. The devices were measured both in the reverse scan (1.2 to -0.05 V, step 0.01 V) and forward scan (-0.05 to 1.2 V, step 0.01 V) with 0.1 V s⁻¹ scan rate. Devices were taken out for EQE measurements using a solar cell spectral response/QE/IPCE measurement system (Solar Cell Scan 100, ZOLIX) with the light intensity being calibrated with a standard single-crystal Si photovoltaic cell. The X-ray diffraction patterns were recorded on a BRUKER ECO D8 series. PL and time resolved PL spectra

were recorded using a spectrofluorometer (FS5, Edinburgh Instruments) and a 405 nm pulsed laser was used as an excitation source for the measurement. Mott-Schottky plots were obtained with an electrochemical workstation (CHI 660E) at 1000 Hz. Electrochemical impedance spectra (EIS) of the cells were obtained using a CHI-660E in the frequency range of 1 Hz to 100 kHz in the dark.

Computational details

The atomic structures of both SnO_2 and $\text{g-C}_3\text{N}_4$ were optimized with density functional theory (DFT) using the Vienna *Ab initio* Simulation Package (VASP). A $\text{g-C}_3\text{N}_4$ molecule (22 atoms) was put on a 4-layer (110) SnO_2 surface, with the unit-cell lattice parameters of the slab model of $12.749 \text{ \AA} \times 13.395 \text{ \AA} \times 23.348 \text{ \AA}$. A vacuum space of 15 \AA thickness was added to the third lattice vector (that is, vertical to the surface) to minimize interactions between neighboring slabs. DFT calculations were performed using the Perdew–Burke–Ernzerhof exchange–correlation functional implemented in the VASP. The energy cutoff was selected to be 500 eV. Both the lattice parameters and the atomic coordinates were optimized until the forces on each atom are less than 0.02 eV \AA^{-1} . The van der Waals interaction between the $\text{g-C}_3\text{N}_4$ molecule and the SnO_2 (110) surface was taken into account *via* a damped vdW correction using the DFT-D3 approach. The Monkhorst-Pack *k*-point sampling was $2 \times 2 \times 1$. Surface dipole correction was employed to avoid artificial interactions between neighboring slabs.

In addition, the charge density differences of the SnO_2 (110) surface upon the formation of an O vacancy were calculated using the relationship

$$\Delta\rho = \rho(\text{SnO}_2) - \rho(\text{O}) - \rho(\text{SnO}_2 \text{ with a vacancy}).$$

To express the interaction between SnO_2 and a $\text{g-C}_3\text{N}_4$ molecule, we also calculated the charge-density change upon the addition of $\text{g-C}_3\text{N}_4$ on the SnO_2 (110) surface using the relationship

$$\Delta\rho = \rho(\text{SnO}_2 \text{ with a vacancy and } \text{g-C}_3\text{N}_4) - \rho(\text{only } \text{SnO}_2 \text{ with a vacancy}) - \rho(\text{only } \text{g-C}_3\text{N}_4).$$

The cyan region represents charge accumulation, and the yellow region indicates charge depletion.

Conflicts of interest

There are no conflicts to declare.

Acknowledgements

This work is financially supported by the National Natural Science Foundation of China (Grant No. 11574248, 61604121, and 61505161), National Key R&D Program of China (Grant No. 2016YFB0400702), Scientific Research Plan Projects of Shaanxi

Education Department (Grant No. 17JK0700), and Natural Science Basic Research Plan in Shaanxi Province of China (Grant No. 2016JM6024 and 2017JM6064). The SEM work was performed at the International Center for Dielectric Research (ICDR), Xi'an Jiaotong University, Xi'an, China. The authors thank Miss Dai/Mr Ma for her/his help in using the SEM. We also thank Dr Liu at the Instrument Analysis Center of Xi'an Jiaotong University for her assistance with UPS analysis.

Notes and references

- 1 A. Kojima, K. Teshima, Y. Shirai and T. Miyasaka, *J. Am. Chem. Soc.*, 2009, **131**, 6050–6051.
- 2 W. S. Yang, B.-W. Park, E. H. Jung, N. J. Jeon, Y. C. Kim, D. U. Lee, S. S. Shin, J. Seo, E. K. Kim, J. H. Noh and S. I. Seok, *Science*, 2017, **356**, 1376–1379.
- 3 https://www.nrel.gov/pv/cell-efficiency.html?tdsourcetag=s_pcqq_aiomsg.
- 4 N. J. Jeon, H. Na, E. H. Jung, T.-Y. Yang, Y. G. Lee, G. Kim, H.-W. Shin, S. I. Seok, J. Seo and J. Lee, *Nat. Energy*, 2018, **3**, 682–689.
- 5 M. Kim, G.-H. Kim, T. K. Lee, I. W. Choi, H. W. Choi, Y. Jo, Y. J. Yoon, J. W. Kim, J. Lee, D. Huh, H. Lee, S. K. Kwak, J. Y. Kim and D. S. Kim, *Joule*, 2019, **3**, 1–14.
- 6 Q. Jiang, Y. Zhao, X. Zhang, X. Yang, Y. Chen, Z. Chu, Q. Ye, X. Li, Z. Yin and J. You, *Nat. Photonics*, 2019, **13**, 460–466.
- 7 H. Dong, J. Xi, L. Zuo, J. Li, Y. Yang, D. Wang, Y. Yu, L. Ma, C. Ran, W. Gao, B. Jiao, J. Xu, T. Lei, F. Wei, F. Yuan, L. Zhang, Y. Shi, X. Hou and Z. Wu, *Adv. Funct. Mater.*, 2019, **29**, 1808119.
- 8 J. Xi, K. Xi, A. Sadhanala, K. H. L. Zhang, G. Li, H. Dong, T. Lei, F. Yu, C. Ran, B. Jiao, P. R. Coxon, C. J. Harrisc, X. Hou, V. R. Kumar and Z. Wu, *Nano Energy*, 2019, **56**, 741–750.
- 9 W. Gao, C. Ran, J. Li, H. Dong, B. Jiao, L. Zhang, X. Lan, X. Hou and Z. Wu, *J. Phys. Chem. Lett.*, 2018, **9**, 6999–7006.
- 10 J. Xi, C. Piao, J. Byeon, J. Yoon, Z. Wu and M. Choi, *Adv. Energy Mater.*, 2019, **9**, 1901787.
- 11 X. T. Meng, X. Cui, M. Rager, S. G. Zhang, Z. W. Wang, J. Yu, Y. W. Harn, Z. T. Kang, B. K. Wagner, Y. Liu, C. Yu, J. S. Qiu and Z. Q. Lin, *Nano Energy*, 2018, **52**, 123–133.
- 12 M. He, B. Li, X. Cui, B. B. Jiang, Y. J. He, Y. H. Chen, D. O'Neil, P. Szymanski, M. A. El-Sayed, J. S. Huang and Z. Q. Lin, *Nat. Commun.*, 2017, **8**, 16045.
- 13 M. D. Ye, C. F. He, J. Iocozzia, X. Q. Liu, X. Cui, X. T. Meng, M. Rager, X. D. Hong, X. Y. Liu and Z. Q. Lin, *J. Phys. D: Appl. Phys.*, 2017, **50**, 373002.
- 14 M. He, X. C. Pang, X. Q. Liu, B. B. Jiang, Y. J. He, H. Snaith and Z. Q. Lin, *Angew. Chem., Int. Ed.*, 2016, **55**, 4280–4284.
- 15 D. Cruz, J. G. Cerrillo, B. Kumru, N. Li, J. D. Perea, B. V. K. J. Schmidt, I. Lauermann, C. J. Brabec and M. Antonietti, *J. Am. Chem. Soc.*, 2019, **141**, 12322–12328.
- 16 M. He, D. J. Zheng, M. Y. Wang, C. J. Lin and Z. Q. Lin, *J. Mater. Chem. A*, 2014, **2**, 5994–6003.
- 17 F. Wei, B. Jiao, H. Dong, J. Xu, T. Lei, J. Zhang, Y. Yu, L. Ma, D. Wang, J. Chen, X. Hou and Z. Wu, *J. Mater. Chem. A*, 2019, **7**, 16533–16540.

- 18 J. H. Heo, D. H. Song, H. J. Han, S. Y. Kim, J. H. Kim, D. Kim, H. W. Shin, T. K. Ahn, C. Wolf, T.-W. Lee and S. H. Im, *Adv. Mater.*, 2015, **27**, 3424–3430.
- 19 S. Michael, M. Taisuke, D. Konrad, J.-Y. Seo, U. Amita, M. Z. Shaik, C.-B. Juan-Pablo, R. T. Wolfgang, A. Antonio, H. Anders and M. Grätzel, *Nano Lett.*, 2014, **14**, 2591–2596.
- 20 M. Christopher, S. Patrick, P. Jonathan, A. L. Dmitry and A. Z. Alex, *J. Phys. Chem. C*, 2016, **120**, 6377–6382.
- 21 B. Xia, Z. Wu, H. Dong, J. Xi, W. Wu, T. Lei, K. Xi, F. Yuan, B. Jiao, L. Xiao, Q. Gong and X. Hou, *J. Mater. Chem. A*, 2016, **4**, 6295–6303.
- 22 W. Ke, G. Fang, Q. Liu, L. Xiong, P. Qin, H. Tao, J. Wang, H. Lei, B. Li, J. Wan, G. Yang and Y. Yan, *J. Am. Chem. Soc.*, 2015, **137**, 6730–6733.
- 23 B. Zhao, G. Niu, Q. Dong, J. Liu, N. Li, J. Li and L. Wang, *J. Mater. Chem. A*, 2018, **6**, 23797–23804.
- 24 M. T. Mohammad, S. Michael, Y. Pankaj, H. Philippe, H. Anders, M. Z. Shaik and G. Michael, *Adv. Energy Mater.*, 2019, **9**, 1802646.
- 25 X. Liu, K.-W. Tsai, Z. Zhu, Y. Sun, C.-C. Chueh and K.-Y. J. Alex, *Adv. Mater. Interfaces*, 2016, **3**, 1600122.
- 26 G. Yang, C. Chen, F. Yao, Z. Chen, Q. Zhang, X. Zheng, J. Ma, H. Lei, P. Qin, L. Xiong, W. Ke, G. Li, Y. Yan and G. Fang, *Adv. Mater.*, 2018, **30**, 1706023.
- 27 G. G. Kate, W. Aron and W. W. Graeme, *J. Phys. Chem. C*, 2009, **113**, 439–448.
- 28 A. Kar, S. Kundu and A. Patra, *J. Phys. Chem. C*, 2011, **115**, 118–124.
- 29 F. Gu, S. Wang, M. K. Lu, G. J. Zhou, D. Xu and D. R. Yuan, *J. Phys. Chem. B*, 2004, **108**, 8119–8123.
- 30 J. Xie, K. Huang, X. Yu, Z. Yang, Ke. Xiao, Y. Qiang, X. Zhu, L. Xu, P. Wang, C. Cui and D. Yang, *ACS Nano*, 2017, **11**, 9176–9182.
- 31 J. Xu, T. Brenner, L. Chabanne, D. Neher, M. Antonietti and M. Shalom, *J. Am. Chem. Soc.*, 2014, **136**, 13486–13489.
- 32 D. Cruz, J. Cerrillo, B. Kumru, N. Li, J. Perea, B. Schmidt, I. Lauermann, C. Brabec and M. Antonietti, *J. Am. Chem. Soc.*, 2019, **141**, 12322–12328.
- 33 Q. Cui, J. Xu, X. Wang, L. Li, M. Antonietti and M. Shalom, *Angew. Chem., Int. Ed.*, 2016, **55**, 3672–3676.
- 34 J. Liu, H. Wang and M. Antonietti, *Chem. Soc. Rev.*, 2016, **45**, 2308–2326.
- 35 B. Tu, Y. Shao, W. Chen, Y. Wu, X. Li, Y. He, J. Li, F. Liu, Z. Zhang, Y. Lin, X. Lan, L. Xu, X. Shi, A. M. Ching, H. Li, L. W. Chung, B. D. Aleksandra and Z. He, *Adv. Mater.*, 2019, **31**, 1805944.
- 36 H. Chen, D. Liu, Y. Wang, C. Wang, T. Zhang, P. Zhang, H. Sarvari, Z. Chen and S. Li, *Nanoscale Res. Lett.*, 2017, **12**, 238.
- 37 X. Ren, D. Yang, Z. Yang, J. Feng, X. Zhu, J. Niu, Y. Liu, W. Zhao and F. S. Liu, *ACS Appl. Mater. Interfaces*, 2017, **9**, 2421–2429.
- 38 E. H. Anaraki, A. Kermanpur, M. T. Mayer, L. Steier, T. Ahmed, S.-H. Turren-Cruz, J. Seo, J. Luo, S. M. Zakeeruddin, W. R. Tress, T. Edvinsson, M. Grätzel, A. Hagfeldt and J.-P. Correa-Baena, *ACS Energy Lett.*, 2018, **3**, 773–778.
- 39 B. Roose, M. C. Johansen, K. Dupraz, T. Jaouen, P. Aebi, U. Steiner and A. A. Abate, *J. Mater. Chem. A*, 2018, **6**, 1850–1857.
- 40 M. Park, J.-Y. Kim, H. J. Son, C.-H. Lee, S. Jang and M. J. Ko, *Nano Energy*, 2016, **26**, 208–215.
- 41 G. Yang, H. Lei, H. Tao, X. Zheng, J. Ma, Q. Liu, W. Ke, Z. Chen, L. Xiong, P. Qin, Z. Chen, M. Qin, X. Lu, Y. Yan and G. Fang, *Small*, 2017, **13**, 1601769.
- 42 Y. Bai, Y. Fang, Y. Deng, Q. Wang, J. Zhao, X. Zheng, Y. Zhang and J. Huang, *ChemSusChem*, 2016, **9**, 2686–2691.
- 43 D. Yang, R. Yang, K. Wang, C. Wu, X. Zhu, J. Feng, X. Ren, G. Fang, S. Priya and F. S. Liu, *Nat. Commun.*, 2018, **9**, 3239.
- 44 J. Wei, F. Guo, X. Wang, K. Xu, M. Lei, Y. Liang, Y. Zhao and D. Xu, *Adv. Mater.*, 2018, **30**, 1805153.
- 45 K. Liu, S. Chen, J. Wu, H. Zhang, M. Qin, X. Lu, Y. Tu, Q. Meng and X. Zhan, *Energy Environ. Sci.*, 2018, **11**, 3463–3471.
- 46 W.-J. Ong, L.-L. Tan, Y. H. Ng, S.-T. Yong and S.-P. Chai, *Chem. Rev.*, 2016, **116**, 7159–7329.
- 47 Q. Jiang, L. Zhang, H. Wang, X. Yang, J. Meng, H. Liu, Z. Yin, J. Wu, X. Zhang and J. You, *Nat. Energy*, 2016, **2**, 16177.
- 48 P. Kumar, E. Vahidzadeh, U. K. Thakur, P. Kar, K. M. Alam, A. Goswami, N. Mahdi, K. Cui, G. M. Bernard, V. K. Michaelis and K. Shankar, *J. Am. Chem. Soc.*, 2019, **141**, 5415–5436.
- 49 K. Yao, F. Li, Q. He, X. Wang, Y. Jiang, H. Huang and A. K.-Y. Jen, *Nano Energy*, 2017, **40**, 155–162.
- 50 Q. Dong, J. Li, Y. Shi, M. Chen, L. K. Ono, K. Zhou, C. Zhang, Y. Qi, Y. Zhou, N. P. Padture and L. Wang, *Adv. Energy Mater.*, 2019, **9**, 1900834.
- 51 J. W. Jung, C.-C. Chueh and A. K.-Y. Jen, *Adv. Energy Mater.*, 2015, **5**, 1500486.
- 52 J. Duan, Y. Zhao, B. He and Q. Tang, *Angew. Chem., Int. Ed.*, 2018, **57**, 3787–3791.
- 53 W. Chen, Y. Wu, J. Fan, A. B. Djurišić, F. Liu, H. W. Tam, A. Ng, C. Surya, W. K. Chan, D. Wang and Z.-B. He, *Adv. Energy Mater.*, 2018, **8**, 1703519.
- 54 S. R. Cowan, A. Roy and A. J. Heeger, *Phys. Rev. B: Condens. Matter Mater. Phys.*, 2010, **82**, 245207.
- 55 Y. Shao, Y. Yuan and J. Huang, *Nat. Energy*, 2016, **1**, 15001.
- 56 G. Kresse and J. Hafner, *Phys. Rev. B: Condens. Matter Mater. Phys.*, 1994, **49**, 14251–14269.
- 57 G. Kresse and J. Furthmüller, *Comput. Mater. Sci.*, 1996, **6**, 15–50.
- 58 G. Kresse and J. Furthmüller, *Phys. Rev. B: Condens. Matter Mater. Phys.*, 1996, **54**, 11169–11186.
- 59 J. P. Perdew, K. Burke and K. Ernzerhof, *Phys. Rev. Lett.*, 1996, **77**, 3865–3868.
- 60 P. E. Blöchl, *Phys. Rev. B: Condens. Matter Mater. Phys.*, 1994, **50**, 17953–17979.
- 61 S. Grimme, J. Antony, S. Ehrlich and H. A. Krieg, *J. Chem. Phys.*, 2010, **132**, 154104.
- 62 J. Liu, *J. Phys. Chem. C*, 2015, **119**, 28417–28423.
- 63 J. Wang, Z. Guan, J. Huang, Q. Li and J. Yang, *J. Mater. Chem. A*, 2014, **2**, 7960–7966.
- 64 L. Zhang, F. Yuan, H. Dong, B. Jiao, W. Zhang, X. Hou, S. Wang, Q. Gong and Z. Wu, *ACS Appl. Mater. Interfaces*, 2018, **10**, 40661–40671.